DOI: 10.1002/((please add manuscript number))
Article type: Communication

Microwave Absorption of Organic Metal Halide Nanotubes

Haoran Lin, Michael Green, Liang-Jin Xu, Xiaobo Chen, Biwu Ma**

Dr. Haoran Lin, Dr. Liang-Jin Xu, Prof. Biwu Ma[*]
Department of Chemistry and Biochemistry, Florida State University, Tallahassee, FL 32306
E-mail: bma@fsu.edu

Dr. Haoran Lin
Hoffmann Institute of Advanced Materials, Shenzhen Polytechnic, 7098 Liuxian Boulevard, Nanshan District, Shenzhen 518055, P.R. China

Michael Green, Prof. Xiaobo Chen[*]
Department of Chemistry, University of Missouri – Kansas City, Kansas City, MO 64110
E-mail: chenxiaobo@umkc.edu

Keywords: Organic metal halide hybrids, nanotubes, microwave absorption, electromagnetic properties

Abstract:

Organic metal halide hybrids have attracted tremendous research interests owing to their outstanding optical and electronic properties suitable for various applications, including photovoltaics, light-emitting diodes and photodetectors. Recently, the multifunctionality of this class of materials has been further explored beyond their optical and electronic properties. Here, we report for the first time the microwave electromagnetic properties of a one-dimensional (1D) organic metal halide hybrid, $(C_6H_{13}N_4)_3Pb_2Br_7$, a single crystalline bulk assembly of organic metal halide nanotubes. Good microwave absorption performance with a large reflection loss value of -18.5 dB and a threshold bandwidth of 1.0 GHz was discovered for this material, suggesting its potential as a new microwave absorber. This work has revealed a new functionality of organic metal halide hybrids and provides a new material class for microwave absorption application studies.

Organic metal halide hybrids refer to an important class of materials with exceptional versatile functionalities. They have been intensively investigated in recent years for their outstanding performance in optoelectronic devices, such as photovoltaics, light-emitting diodes, photodetectors *etc*.[1] By tuning the material combinations of organic and inorganic metal halides, formation of organic metal halide hybrids with different dimensionalities at the molecular level can be achieved. Determined by the nanostructures of the metal halide backbones in the corresponding crystalline bulk assemblies, molecular low-dimensional organic metal halide hybrids are defined to be two- (2D), one- (1D) and zero-dimensional (0D) materials.[2] The 1D family among them, exhibits prominent structural versatility. For instance, 1D metal halide hybrids can form linear, zig-zag, ribbon-shape, corrugated and even tubular structures.[3] Recently, we reported an organic metal halide hybrid $(C_6H_{13}N_4)_3Pb_2Br_7$ with a unique tubular structure, as shown in Figure 1.[3d] The single crystal contains parallel arrays of 1D lead bromide nanotubes with organic cations ionically bonded to the surfaces inside and out. Since the metal halide nanotubes are spatially isolated from each other, there is negligible inter-tubular interaction and band dispersion, so that the intrinsic properties of an individual nanotube can be manifested by its bulk assembly. This 1D organic metal halide hybrid have been reported to exhibits yellowish-white emission with exciton-exciton annihilation, and with good stability.[3d, 4] Considering the vast functionalities of other nanotube materials, such as carbon nanotubes (CNTs),[5] we believed that this unique bulk assembly of 1D organic metal halide nanotubes (OMHNT's) could have multiple functionalities besides its intriguing optical properties.

Microwave absorbing materials are important components for many military and civil applications, such as anti-radar detection and wireless communications,[6] used in order to reduce the radar signature and electromagnetic interference of various equipment. To date, a variety types of materials have been investigated, including graphite,[7] graphene,[6b, 8] CNTs,[9] carbon fiber,[10] conducting polymers,[11] Fe_2O_3,[12] Fe_3O_4,[13] MnO_2,[14] ZnO,[15] TiO_2,[6c, 16]

$BaFe_{12}O_{19}$,[17] $BaTiO_3$,[18] $SrFe_{12}O_{19}$,[19] SiC,[20] SiCN,[21] Co_2P,[22] FeP,[23] g-C_3N_4,[24] SiO_2,[25] MOF's,[26a] POM's,[26b] *et alia*. In this work, we first time investigate and report the microwave dielectric and magnetic properties and microwave absorption performance of the 1D organic metal halide hybrid $(C_6H_{13}N_4)_3Pb_2Br_7$. The microwave absorption performance is analyzed in detail, in terms of the reflection loss peak frequency (f_{peak}), reflection loss peak value (RL_{peak}), the critical reflection loss peak width (Δf_{10}), and their relationships with the thickness of the absorber (d). Our study not only enriches the knowledge of organic metal halide hybrids, but also provides a potential new class of materials for microwave absorption.

The $(C_6H_{13}N_4)_3Pb_2Br_7$ crystals were prepared by solvent diffusion method (see experimental section). To confirm the structure of the as-prepared material, we performed powder X-ray diffraction (PXRD) experiment and found the PXRD pattern is identical with the simulated result from $(C_6H_{13}N_4)_3Pb_2Br_7$ single crystal X-ray diffraction (SCXRD) data (Figure 2A). Excitation and steady-state photoluminescence spectra of the prepared crystals were also measured at room temperature showing a UV range excitation and a broad band yellowish white emission (Figure 2B), which are in accordance with the previously reported results.[3d] The SEM image of the organic metal halide hybrid in Figure S1 displayed a regular needle shape, with a smooth crystal surface for the grinded $(C_6H_{13}N_4)_3Pb_2Br_7$ crystals.

We then characterized the electromagnetic properties of $(C_6H_{13}N_4)_3Pb_2Br_7$ nanotubes (see experimental section) for materials dispersed in paraffin substrate at 15wt%, 30wt%, and 60wt%. Analysis by wt% showed that the bulk dielectric and magnetic parameters of the analytes increased in a general linear fashion when contrasted with paraffin's bulk electromagnetic properties [26b] as shown in Figure S2 and Figure S3. For the 60wt%, Figure. 3A showed the complex permittivity parameters of the $(C_6H_{13}N_4)_3Pb_2Br_7$ nanotubes. ε' was between 3.52 and 3.41; ε'' decreased from 0.35 to 0.05 from 1.0 to 9.0 GHz and subsequently increased to 0.12 at 18.0 GHz; $tg\delta_\varepsilon$ was determined to be 0.10 at 1.0 GHz, from where it

decreased to 0.014 at 9.0 GHz, and then increased to 0.034 at 18.0 GHz. Figure. 3B exhibited the complex permeability parameters. μ' fluctuated between 1.01 and 0.95, μ'' and tgδ_μ decreased from 0.33 to about 0.03 from 1.0 to 18.0 GHz. These small μ'' and tgδ_μ parameters indicate that the energy lost within the nanotubes due to magnetic interaction is small, though the lossy dielectric and magnetic interactions were of similar magnitude.

Figure 3C plotted the electrical conductivity (σ) of the $(C_6H_{13}N_4)_3Pb_2Br_7$ nanotubes. σ was obtained from σ(S/m) = $2\pi f\varepsilon_0\varepsilon''$, where ε_0, f and ε'' were the free space permittivity constant (8.854×10^{-12} F/m), the frequency (Hz), and the imaginary component of permittivity, respectively.[27] σ increased from 0.020 S/m at 1.0 GHz to 0.12 S/m at 18.0 GHz, with some fluctuation. The small σ value indicated the weak electrical conductivity of the $(C_6H_{13}N_4)_3Pb_2Br_7$ nanotubes which is supported by the previous theoretical calculations.[3d] The skin-depth (δ) was displayed in Figure 3D. δ was obtained from (δ/m) = $(\pi f\mu_0\mu_r\sigma)^{-1/2}$, where μ_0, μ_r and σ are the permeability of free space ($4\pi \times 10^{-7}$ H/m), the relative permeability, and the electrical conductivity (S/m), respectively.[27] The value of δ decreased from 114.6 at 1.0 GHz to around 11.0 *mm* at 18.0 GHz. Apparently, σ increased but δ decreased with the frequency. The large δ values indicated the poor damping of the incident microwave irradiation inside the $(C_6H_{13}N_4)_3Pb_2Br_7$ nanotubes.

The $(C_6H_{13}N_4)_3Pb_2Br_7$ nanotubes' microwave absorption properties were evaluated with equation (1) and (2).

$$RL(\text{dB}) = 20 \log |(Z_{in} - Z_0)/(Z_{in} + Z_0)| \quad (1)$$

$$Z_{in}(f, d) = Z_0(\mu_r/\varepsilon_r)^{1/2}\tanh[j(2\pi f{\cdot}d/c)\,(\varepsilon_r\mu_r)^{1/2}] \quad (2)$$

Here RL(dB), Z_{in} and Z_0 are the reflection loss (dB), the absorber's input impedance, and the free space's impedance, respectively; μ_r, and ε_r are the relative complex permeability and permittivity, respectively; f, d and c are the microwave frequency, the absorber's thickness and the light's velocity.[15b, 16, 28] RL evolved with f and d in Figure 4A with four absorption bands

of increasing *RL* values as *d* increased, as also seen in Figure 4B's contour plot. *RL* was smaller than -10 dB when *d* was less than 11.0 *mm* or *f* was less than 10.0 GHz. There were two narrow bands with *RL* larger than -10 dB when *d* was between 11.0 to 20.0 *mm* and *f* was between 10.0 to 18.0 GHz. Figure 4C showed some typical *RL* curve of those four bands as *d* changed. *RL* was larger than -10 dB only for bands 3 and 4 in some *f* and *d* ranges. Figure 4D displayed the changes of f_{peak} with *d*. Band1 to band4 gradually appeared as *d* was increased to about 3.5, 6.9, 11.5, and 16.0 *mm*, respectively. All f_{peak} values decrease with *d* with the relationships $f_{peak1} = c/4dn$, $f_{peak2} = 3c/4dn$, $f_{peak3} = 5c/4dn$, and $f_{peak4} = 7c/4dn$ where c and *n* was the light's speed and the materials' refractive index, and *n* was obtained from $n = \mathrm{Re}[(\varepsilon_r\mu_r)^{1/2}]$.[28] or in other words $d = c/4nf_{peak1} = \lambda/4$, $d = 3c/4nf_{peak2} = 3\lambda/4$, $d = 5c/4nf_{peak3} = 5\lambda/4$, and $d = 7c/4nf_{peak4} = 7\lambda/4$. Maximum reflection loss was observed whenever *d* was odd ($2m$-1, m = 1, 2, …positive integer) folds of the quarter wavelength (λ/4,) in the materials. That was because the microwave reflected from the front surface were largely cancelled by the microwave reflected from the back surface. RL_{peak} was plotted against *d* in Figure 4E. *RL* increased with *d*. *RL* values decreased from band4 to band3, band2 and band1. RL_{peak} was smaller than -10 dB for band1 and band2, while larger than -10 dB for *d* of 13.3-20.0 *mm* and 18.2-20.0 *mm* for band3 and band4, respectively. A maximum RL_{peak} value of -18.45 dB was obtained near d = 16.1 *mm* in band4. Figure 4F plotted the Δf_{10} vs *d*. No curves were observed for band1 and band2 because these bands had no *RL* values larger than -10 dB. Band3 had Δf_{10} between 0.17 to 0.5 GHz when *d* was 11.3 to 20.0 *mm*, and band4 showed Δf_{10} of 0.17 to 1.0 GHz with *d* of 15.7 to 20.0 *mm*. Using the observed trends in wt%, we generated a permittivity and permeability model so to simulate the intrinsic material response to incident electromagnetic radiation. These results are shown in Figure S4, Figure S5, and Figure S6 for the band analysis, reflection loss, and response profile. The results of these models suggest that the permittivity and permeability values of the intrinsic materials increase as wt% increases, are capable of strong microwave absorption with

capable effective bandwidths, greater than -50 dB and 3GHz respectively, which is of similar the strengths and breadths as compared to other halide perovskites presented in the literature.[29] As microwave absorption is commonly understood to be from dipole rotation caused electrical loss or magnetic domain resonance caused magnetic loss, it is therefore necessary to reveal the contributions of the electrical and magnetic losses to the microwave absorption properties. In order to understand the contributions from the electrical dissipation pathway in the $(C_6H_{13}N_4)_3Pb_2Br_7$ nanotubes, *RL* was evaluated with zero ε'' and averaged ε' over the entire frequency range. This seemed reasonable as ε' fluctuated only within 3.42 - 3.51. Figure 5A showed the 3D *RL* plots. There were four *RL*-increasing bands with *d* with almost no *RL* larger than -10 dB across the frequency and thickness regions. Only three scattered small bands were observed at large *f* and *d* values, as shown in Figure 5B, the contour plot. Figure 5C displayed some representative *RL* curves, and Figure 5D plotted the f_{peak} values. The bands 1-4 gradually emerged as *d* grew to around 5.6, 6.9, 11.5, and 16.0 *mm*, respectively. All f_{peak} values decreased again as $f_{peak1} = c/4dn$, $f_{peak2} = 3c/4dn$, $f_{peak3} = 5c/4dn$, and $f_{peak4} = 7c/4dn$. Figure 5E exhibited the plots of RL_{peak} vs *d*. All bands had *RL* smaller than -10 dB and the largest *RL* was only -8.28 dB. A monochromic *RL* increase with *d* was observed only band1, not for other bands. No discernable Δf_{10} curves were observed, as *RL* was smaller than -10 dB. Apparently, RL_{peak} largely decreased as ε'' became zero. This indicated a large contribution from the electrical loss of the $(C_6H_{13}N_4)_3Pb_2Br_7$ nanotubes to their microwave absorption performance.

In order to discern the contribution of the magnetic properties of $(C_6H_{13}N_4)_3Pb_2Br_7$ nanotubes to their microwave absorption performance, *RL* was obtained with zero χ_m, where $\mu_r = \mu/\mu_0 = (1+\chi_m)\mu_0$. The 3D plot in Figure 6A showed how *RL* evolved with *f* and *d* when $\chi_m = 0$. Four absorption bands gradually appeared with *d*. However, all *RL* was smaller than -10 dB, also seen in Figure 6B, the contour plot. Some representative *RL* curves were displayed Figure 6C when *d* increased from 1.0 to 18.0 *mm*. No curves had RL_{peak} value larger than -10 dB. Figure

6D plotted the f_{peak} values. Band1 to band4 gradually came out when d grew to around 5.6, 6.8, 11.2, and 15.6 mm, respectively. All f_{peak} decreased with d, again as $f_{peak1} = c/4dn$, $f_{peak2} = 3c/4dn$, $f_{peak3} = 5c/4dn$, and $f_{peak4} = 7c/4dn$. The plots Figure 6E indicated that band 4 had the largest RL values, then band3, band2 and band1, and all RL_{peak} was smaller than -10 dB. Furthermore, the largest RL_{peak} was only -6.86 dB. RL increased with d for band1 but decreased for band3 and band4. No discernable Δf_{10} curves were observed, as RL was smaller than -10 dB. By comparing the results in Figure 4 and Figure 6, it was concluded that RL_{peak} largely decreased as χ_m became zero and none of the conditions could give a RL_{peak} value larger than -10 dB. Therefore, the magnetic loss in the $(C_6H_{13}N_4)_3Pb_2Br_7$ nanotubes also contributed to their microwave absorption performance, just like the electrical loss.

In conjuncture with the simulation analysis, we calculated the Eddy current responses to elucidate the interaction mechanisms. For Eddy current loss, if the Eddy parameter of $C_0 = \mu''/(\mu')^2 \cdot f$ is constant as a function of frequency as specified by the eddy equation,[26b] then magnetism-induced conduction is responsible for the magnetic losses as represented by the permeability. As can be seen in Figure S7, the eddy parameter approaches a low but constant value as frequency increases towards the region of microwave absorption. Such would seem to suggest that eddy currents might be responsible for the magnetic interaction. Similarly, as the dielectric conductivity increases as a function of frequency as seen in Figure 3C, it may be that these conductive responses of the organic metal halide nanotubes are the casual mechanism for microwave absorption,[28] possibly along the length of the nanotubes given the shape factors which are similar to other materials that are conductively microwave active.[28]

In summary, we have evaluated the microwave absorbing properties of an organic metal halide hybrid material $(C_6H_{13}N_4)_3Pb_2Br_7$, which has a large RL of -18.45 dB with a Δf_{10} value of 1.0 GHz. Simulations suggest that the pure OMH demonstrates RL results of greater than -50 dB and bandwidths of greater than 3 GHz. Both the dielectric and magnetic dissipations contribute

to the loss mechanism because the *RL* value decreases largely if the dielectric and magnetic dissipation factors are set to zero. The interference between the incident and reflected microwaves largely determines the effectiveness of the microwave absorption, which is upon the value of the thickness of the coating in comparison to the quarter wavelength of the incident microwave inside the coating which not only depends on the frequency of the microwave but also is intrinsically affected by the dielectric and magnetic constants of $(C_6H_{13}N_4)_3Pb_2Br_7$ through varying conductive interactions. Overall, this work has not only generated new knowledge on the unexplored microwave absorbing property of organic metal halides, but also suggested that organic metal halide materials may have a good potential to work as a completely new class of microwave absorbing materials, while more work is needed to further improve their shielding performance.

Experimental Section

Sample preparation:

Lead (II) bromide and hexamethylenetetramine hydrobromide were mixed at 2:3 molar ratio and dissolved in dimethylformamide to obtain a precursor solution. Needle-shaped $(C_6H_{13}N_4)_3Pb_2Br_7$ crystals were grown by slow diffusing dichloromethane into the precursor solution at room temperature overnight. The crystals were then washed with dichloromethane and subsequently dried under vacuum.

Powder X-ray diffraction analysis:

The PXRD analysis was performed via a Panalytical X'PERT Pro Powder X-Ray Diffractometer using standard Cu X-ray tube radiation at 40 kV and 40 mA, and a X'Celerator RTMS detector. The material was irradiated over an angular range of 5-60 degrees 2θ with a 0.02 step size, and the analysis was done at room temperature.

Simulated powder diffraction patterns were calculated via Mercury software using the resulting crystallographic information file (CIF) file resulting from the SCXRD experiment.

Photoluminescence steady state studies:

Excitation and emission spectra of $(C_6H_{13}N_4)_3Pb_2Br_7$ single crystals were measured at room temperature on a FS5 spectrofluorometer (Edinburgh Instruments). The excitation spectra were monitored at 700 nm and the emission spectra were obtained by using excitation wavelength of 360 nm generated by a Xenon lamp.

Microwave performance measurements:

An HP8722ES network analyzer was used to measure the complex permittivity and permeability in the frequency range of 1.0–18.0 GHz. The $(C_6H_{13}N_4)_3Pb_2Br_7$ nanotubes were dispersed in paraffin wax with 60 wt%. The composite was molded into small rings with thicknesses on the order of 1.0–4.0 *mm*, with inner and outer diameters of the ring being 3.0 *mm* and 7.0 *mm*, respectively. The pellet thickness was controlled by polishing the pellet after preparation. All the related measurements were conducted at room temperature.

Acknowledgements
H. L., L. X. and B. M. acknowledge the support from the National Science Foundation (DMR-1709116) and the Air Force Office of Scientific Research (AFOSR) (17RT0906). M.G. and X. C. appreciate the support from the National Science Foundation (DMR-1609061).
H. L. and M. G. contribute equally to this work.

Received: ((will be filled in by the editorial staff))
Revised: ((will be filled in by the editorial staff))
Published online: ((will be filled in by the editorial staff))

References

[1] a) J. S. Manser, J. A. Christians, P. V. Kamat, *Chem. Rev.* **2016**, *116*, 12956-13008; b) P. Chen, Y. Bai, M. Q. Lyu, J. H. Yun, M. M. Hao, L. Z. Wang, *Sol. RRL* **2018**, *2*, 1700186.

[2] C. Zhou, H. Lin, Q. He, L. Xu, M. Worku, M. Chaaban, S. Lee, X. Shi, M.-H. Du, B. Ma, *Mater. Sci. Eng., R* **2019**, *137*, 38-65.

[3] a) Z. Tang, A. M. Guloy, *J. Am. Chem. Soc.* **1999**, *121*, 452-453; b) M. E. Kamminga, G. A. de Wijs, R. W. A. Havenith, G. R. Blake, T. T. M. Palstra, *Inorg. Chem.* **2017**, *56*, 8408-8414; c) Z. Yuan, C. Zhou, Y. Tian, Y. Shu, J. Messier, J. C. Wang, L. J. van de Burgt, K. Kountouriotis, Y. Xin, E. Holt, K. Schanze, R. Clark, T. Siegrist, B. Ma, *Nat. Commun.* **2017**, *8*, 14051; d) H. Lin, C. Zhou, Y. Tian, T. Besara, J. Neu, T. Siegrist, Y. Zhou, J. Bullock, K. S. Schanze, W. Ming, M. H. Du, B. Ma, *Chem. Sci.* **2017**, *8*, 8400-8404; e) H. Lin, C. Zhou, J. Neu, Y. Zhou, D. Han, S. Chen, M. Worku, M. Chaaban, S. Lee, E. Berkwits, T. Siegrist, M.-H. Du, B. Ma, *Adv. Opt. Mater.* **2019**, 1801474; f) R. Gautier, F. Massuyeau, G. Galnon, M. Paris, *Adv. Mater.* **2019**, 1807383.

[4] Y. Z. Ma, H. Lin, M. H. Du, B. Doughty, B. Ma, *J. Phys. Chem. Lett.* **2018**, *9*, 2164-2169.

[5] R. H. Baughman, A. A. Zakhidov, W. A. de Heer, *Science* **2002**, *297*, 787-792.

[6] a) J. Y. Dong, R. Ullal, J. Han, S. H. Wei, X. Ouyang, J. Z. Dong, W. Gao, *J. Mater. Chem. A* **2015**, *3*, 5285-5288; b) Y. Zhang, Y. Huang, T. Zhang, H. Chang, P. Xiao, H. Chen, Z. Huang, Y. Chen, *Adv. Mater.* **2015**, *27*, 2049-2053; c) T. Xia, C. Zhang, N. A. Oyler, X. Chen, *Adv. Mater.* **2013**, *25*, 6905-6910.

[7] Y. Z. Fan, H. B. Yang, M. H. Li, G. T. Zou, *Mater. Chem. Phys.* **2009**, *115*, 696-698.

[8] X. Bai, Y. H. Zhai, Y. Zhang, *J. Mater. Chem. C* **2011**, *115*, 11673-11677.

[9] a) Z. F. Liu, G. Bai, Y. Huang, F. F. Li, Y. F. Ma, T. Y. Guo, X. B. He, X. Lin, H. J. Gao, Y. S. Chen, *J. Mater. Chem. C* **2007**, *111*, 13696-13700; b) M. H. Al-Saleh, W. H. Saadeh, U. Sundararaj, *Carbon* **2013**, *60*, 146-156.

[10] L. Liu, K. Zhou, P. He, T. Chen, *Mater. Lett.* **2013**, *110*, 76-79.

[11] a) L. Olmedo, P. Hourquebie, F. Jousse, *Adv. Mater.* **1993**, *5*, 373-377; b) K. Lakshmi, H. John, K. T. Mathew, R. Joseph, K. E. George, *Acta Materialia* **2009**, *57*, 371-375.

[12] G. Sun, B. Dong, M. Cao, B. Wei, C. Hu, *Chem. Mater.* **2011**, *23*, 1587-1593.

[13] K. Jia, R. Zhao, J. C. Zhong, X. B. Liu, *J. Magn. Magn. Mater.* **2010**, *322*, 2167-2171.

[14] M. Zhou, X. Zhang, J. Wei, S. Zhao, L. Wang, B. Feng, *J. Phys. Chem. C* **2010**, *115*, 1398-1402.

[15] a) H. F. Li, Y. H. Huang, G. B. Sun, X. Q. Yan, Y. Yang, J. Wang, Y. Zhang, *J. Mater. Chem. C* **2010**, *114*, 10088-10091; b) T. Xia, Y. Cao, N. A. Oyler, J. Murowchick, L. Liu, X. Chen, *ACS Appl. Mater. Interfaces* **2015**, *7*, 10407-10413.

[16] a) T. Xia, C. Zhang, N. A. Oyler, X. B. Chen, *J. Mater. Res.* **2014**, *29*, 2198-2210; b) L. H. Tian, J. L. Xu, M. Just, M. Green, L. Liu, X. B. Chen, *J. Mater. Chem. C* **2017**, *5*, 4645-4653.

[17] J. X. Qiu, Y. Wang, M. Y. Gu, *Mater. Lett.* **2006**, *60*, 2728-2732.

[18] a) C. C. Yang, Y. J. Gung, W. C. Hung, T. H. Ting, K. H. Wu, *Compos. Sci. Technol.* **2010**, *70*, 466-471; b) L. H. Tian, X. D. Yan, J. L. Xu, P. Wallenmeyer, J. Murowchick, L. Liu, X. B. Chen, *J. Mater. Chem. A* **2015**, *3*, 12550-12556.

[19] P. Kuruva, P. Reddy Matli, B. Mohammad, S. Reddigari, S. Katlakunta, *J. Magn. Magn. Mater.* **2015**, *382*, 172-178.

[20] H. B. Jin, M. S. Cao, W. Zhou, S. Agathopoulos, *Mater. Res. Bull.* **2010**, *45*, 247-250.

[21] Q. Li, X. Yin, W. Duan, B. Hao, L. Kong, X. Liu, *J. Eur. Ceram. Soc.* **2014**, *34*, 589-598.

[22] M. Green, L. Tian, P. Xiang, J. Murowchick, X. Tan, X. Chen, *Mater. Today Nano* **2018**, *1*, 1-7.
[23] M. Green, L. H. Tian, P. Xiang, J. Murowchick, X. Y. Tan, X. B. Chen, *Mater. Chem. Front.* **2018**, *2*, 1119-1125.
[24] M. Green, Z. Liu, R. Smedley, H. Nawaz, X. Li, F. Huang, X. Chen, *Mater. Today Phys.* **2018**, *5*, 78-86.
[25] M. Green, Z. Liu, P. Xiang, Y. Liu, M. Zhou, X. Tan, F. Huang, L. Liu, X. Chen, *Light Sci. Appl.* **2018**, *7*, 87.
[26] a) M. Green, Z. Liu, P. Xiang, X. Tan, F. Huang, L. Liu, X. Chen, *Mater. Today Chem.* **2018**, *9*, 140-148. b) M. Green, Y. Li, Z. Peng, X. Chen, *J. Magn. Magn. Mater.* **2020**, 1, 165974.
[27] D. Micheli, *Radar Absorbing Materials and Microwave Shielding Structures Design: By using Multilayer Composite Materials, Nanomaterials and Evolutionary Computation*, LAP LAMBERT Academic Publishing, **2011**.
[28] M. Green, X. Chen, *J. Mater.* 2019, *5*, 503-514.
[29] H. Guo, J. Yang, B. Pu, H. Chen, Y. Li, Z. Wang, X. Niu, *J. Mater. Chem. C,* **2018**, 6, 4201.

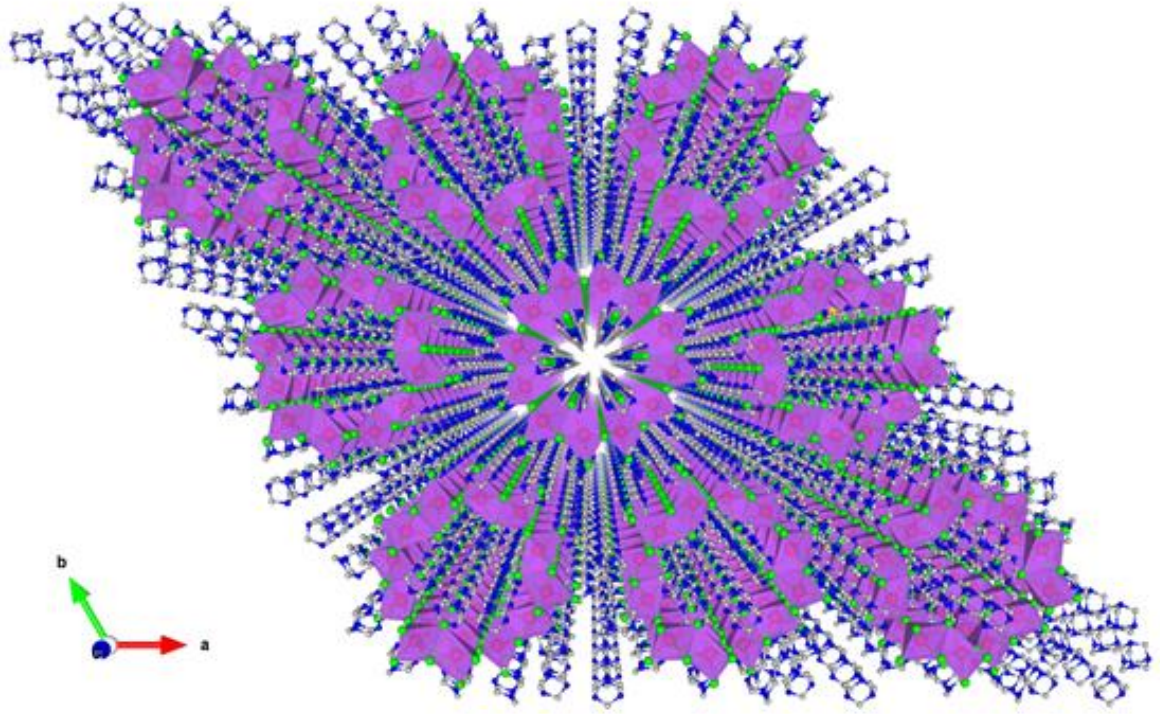

Figure 1. View of the structure of $(C_6H_{13}N_4)_3Pb_2Br_7$ (red: lead atoms; green: bromine atoms; blue: nitrogen atoms; gray: carbon atoms; purple polyhedra: $PbBr_6$ octahedra; hydrogen atoms are hidden for clarity).

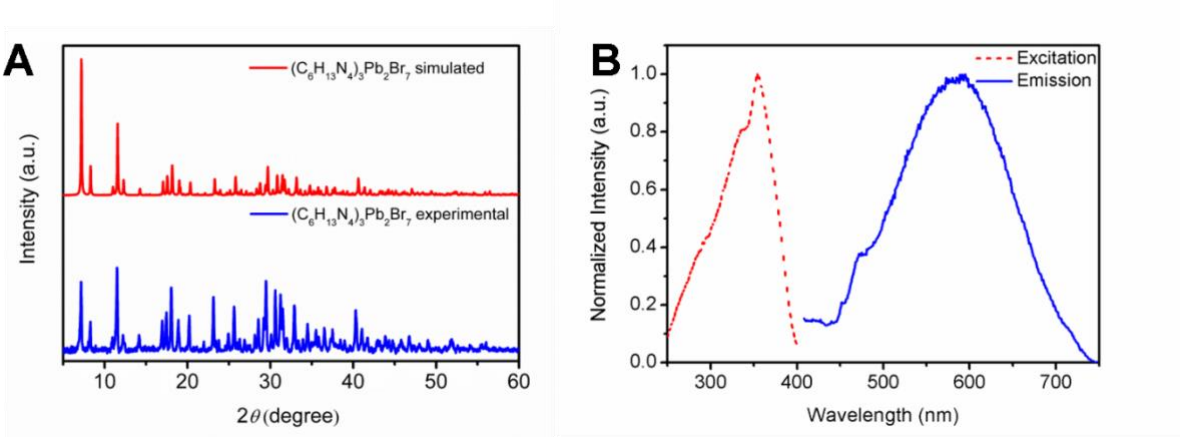

Figure 2. (A) Simulated (red) and experimental (blue) PXRD spectra of $(C_6H_{13}N_4)_3Pb_2Br_7$ nanotubes. (B) Excitation (red dashed line, probe at 700 nm) and emission (blue solid line, excited by 360 nm UV light) spectra of $(C_6H_{13}N_4)_3Pb_2Br_7$ nanotubes.

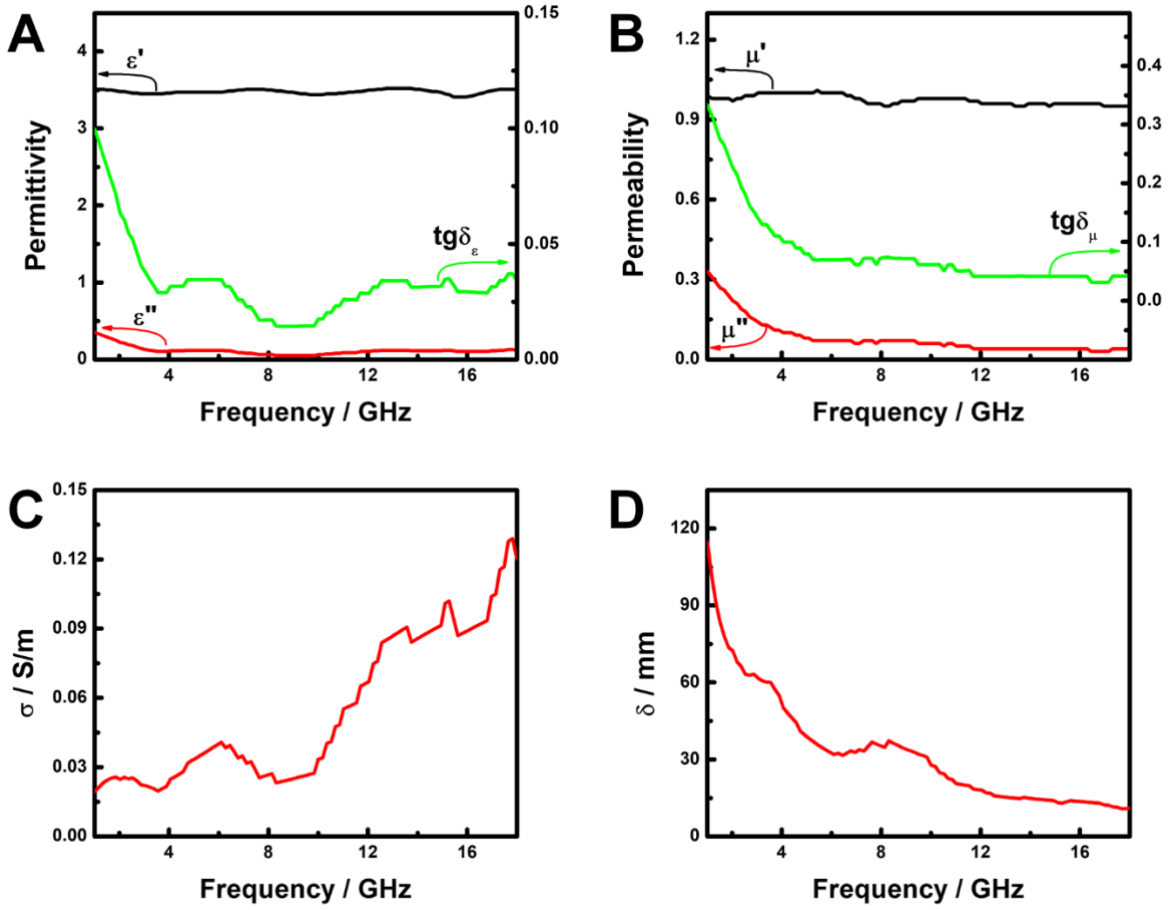

Figure 3. (A) the complex permittivity (ε', ε'', tgδ_ε), (B) complex permeability (μ', μ'', tgδ_μ), (C) microwave conductivity and (D) microwave skin-depth of the nanotubes in the frequency range of 1.0-18.0 GHz.

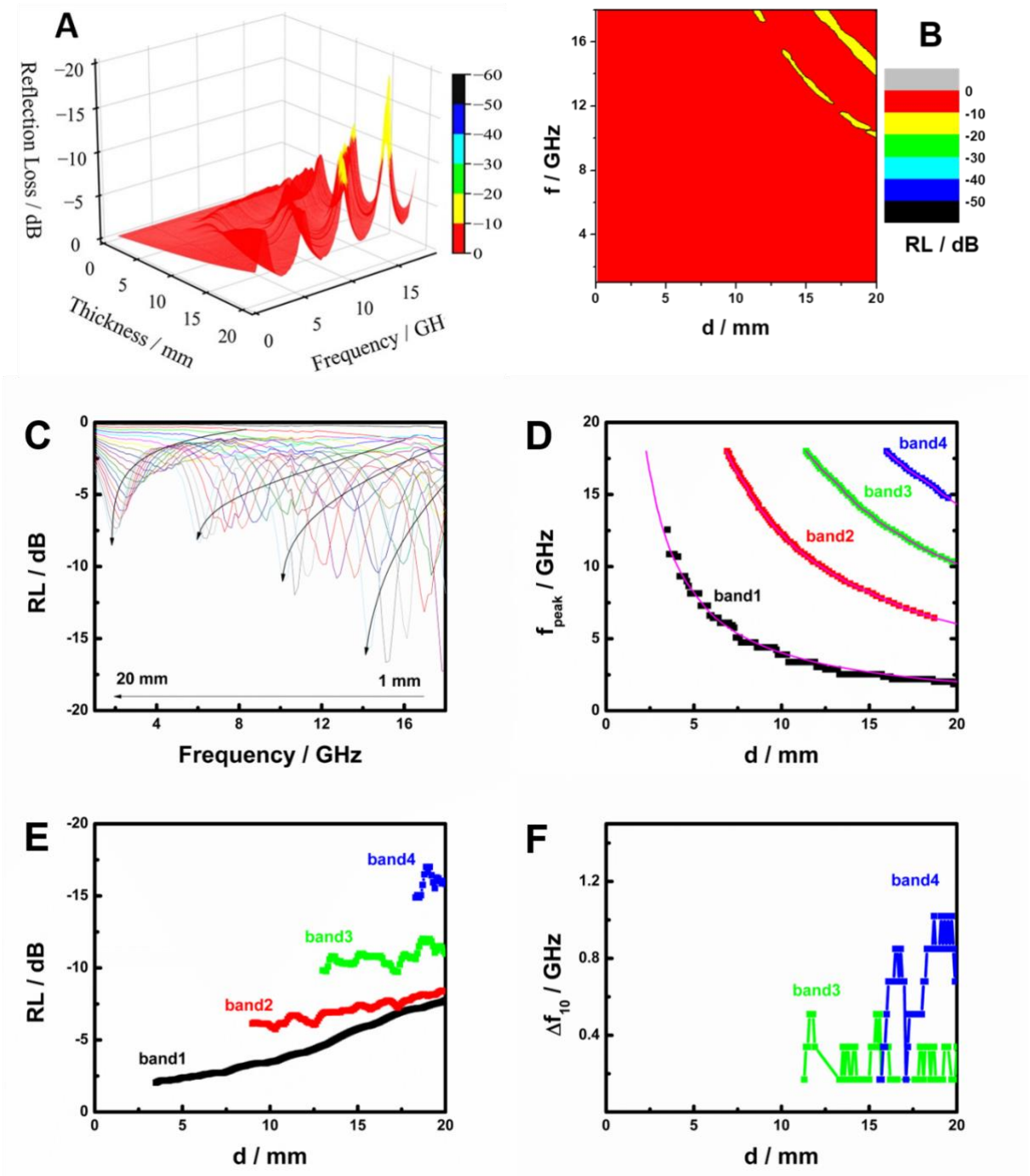

Figure 4. (A) 3D plot, (B) contour plot of *RL* vs. *f* & *d*, (C) The *RL* curves, (D) the relationship of f_{peak}, (E) RL_{peak}, and (F) Δf_{10} with *d*, of the nanotubes. Fig. 4D also shows the fittings of $f_{peak1} = c/4nd$, $f_{peak2} = 3c/4nd$, $f_{peak3} = 5c/4nd$, and $f_{peak4} = 7c/4nd$.

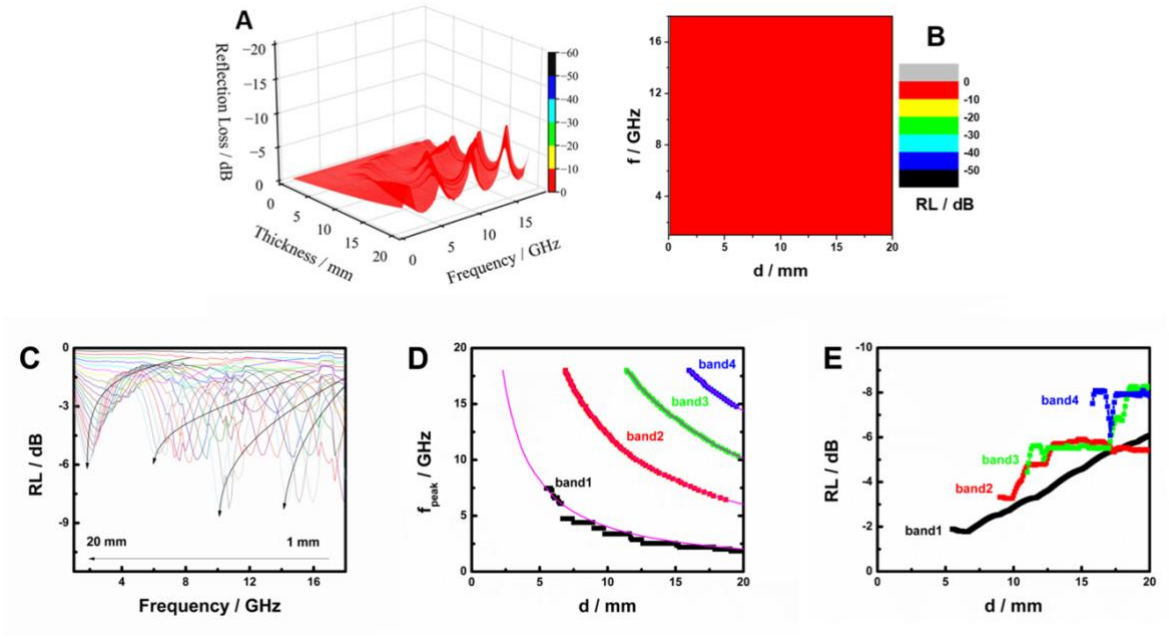

Figure 5. Upon $\varepsilon'' = 0$, (A) 3D plot, (B) contour plot of *RL* vs. f & d, (C) The *RL* curves, (D) the relationship of f_{peak}, and (E) the relationship of RL_{peak}. Fig. 5D also shows the fittings of $f_{peak1} = c/4nd$, $f_{peak2} = 3c/4nd$, $f_{peak3} = 5c/4nd$, and $f_{peak4} = 7c/4nd$.

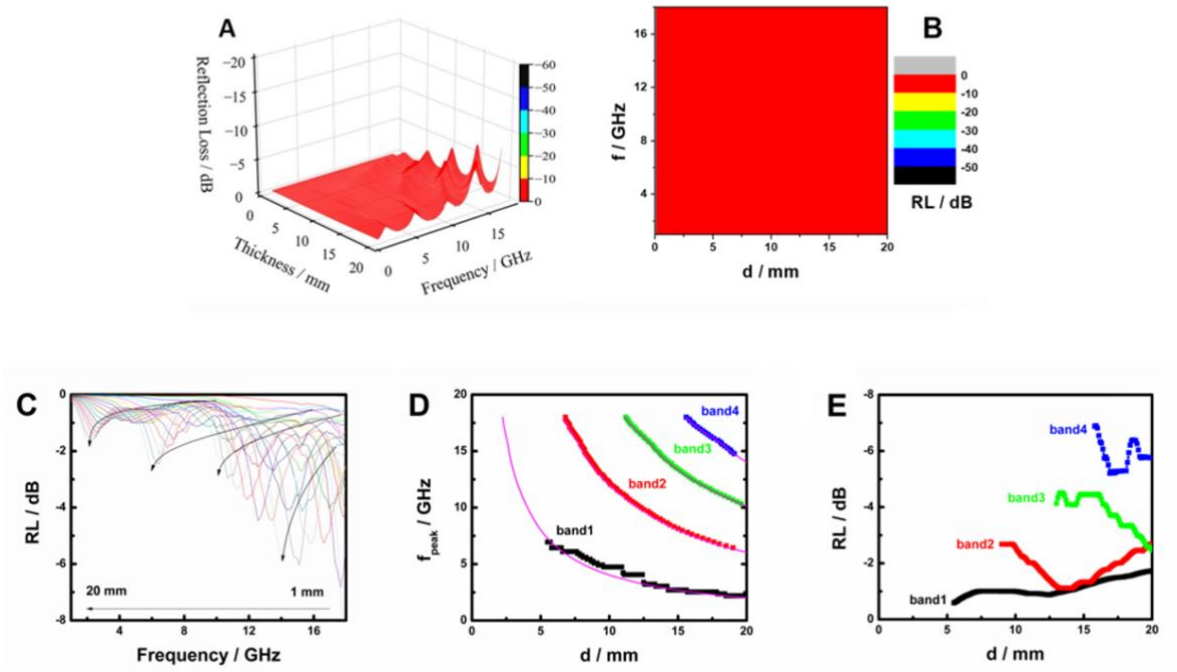

Figure 6. Upon $\chi_m = 0$, (A) 3D plot, (B) contour plot of *RL* vs. *f* & *d*, (C) The *RL* curves, (D) the relationship of f_{peak}, (E) and the relationship of RL_{peak}. Fig. 6D also shows the fittings of $f_{peak1} = c/4nd$, $f_{peak2} = 3c/4nd$, $f_{peak3} = 5c/4nd$, and $f_{peak4} = 7c/4nd$.

The microwave absorbing properties of a one-dimensional organic metal halide hybrid $(C_6H_{13}N_4)_3Pb_2Br_7$ were investigated to exhibit a large reflection loss value of -18.5 dB with a threshold bandwidth of 1.0 GHz. Other than the thickness of the absorbing layer, the intrinsic dielectric and magnetic properties of this material also play important roles to its microwave absorption performance.

Keyword: Organic metal halide hybrids, nanotubes, microwave absorption, electromagnetic properties

Haoran Lin, Michael Green, Liang-Jin Xu, Xiaobo Chen*, Biwu Ma*

Microwave Absorption of Organic Metal Halide Nanotubes

ToC figure